Meas. Sci. Technol. **24** (2013) 065203 (10pp) doi:10.1088/0957-0233/24/6/065203

Measurement of the deformation of an extremely flexible rotor blade using digital image correlation

Jérôme Sicard and Jayant Sirohi

Aerospace Engineering and Engineering Mechanics, The University of Texas at Austin, 210 E 24th Street, Austin, TX 78712, USA

E-mail: jerome.sicard@utexas.edu

Received 29 January 2013, in final form 6 April 2013
Published 14 May 2013
Online at stacks.iop.org/MST/24/065203

Abstract

This paper describes the measurement of the deformation of an extremely flexible rotor blade in hover using a novel application of three-dimensional digital image correlation (3D DIC). In this optical method, images of the rotor blade painted with a high-contrast, random speckle pattern are captured using two digital cameras and a strobe light. Photogrammetry is used to calculate a whole-field, three-dimensional map of the rotor blade. Cross-correlation between images captured under two load conditions is used to calculate deformation. The technique was first validated in the rotating frame by correlating DIC measurements on a stiff rotor blade of known geometry with measurements made by two other laser sensors. The technique was then used to measure the deformation of extremely flexible blades on a 46 cm diameter rotor, rotating at 1200 RPM. The blades of this rotor are so flexible that they can be rolled up into a compact volume. The spanwise variation of extension, lead-lag and flap bending, as well as pitch angle, were extracted from DIC measurements. The technique yielded surface heights with a spatial resolution of 0.15 mm and three-dimensional deformation vectors with a spatial resolution of 2.37 mm (1.04% of the rotor radius), at a calculated accuracy of 15 μm. Tip displacement of up to 7.59 mm (3.3% of the rotor radius) and a tip twist of up to 10.8° were measured. Based on DIC measurements, it is concluded that an accurate aeroelastic model of the rotor blade must include flap and lead-lag bending as well as twist degrees of freedom. In addition, the elastic twist must be considered of the same order of magnitude as the blade root pitch. Finally, the scalability of this technique to the measurement of full-scale rotor blade deformation is discussed.

Keywords: 3D digital image correlation, helicopter blade deformation, flexible rotor blade

(Some figures may appear in colour only in the online journal)

Nomenclature

c	blade chord
DIC	digital image correlation
LDS	laser distance sensor
R	rotor radius
r	radial coordinate
u, v, w	extension, lead-lag bending deflection, flap bending deflection, relative to absolute reference frame
Δu, Δv, Δw	extension, lead-lag bending deflection, flap bending deflection, relative to undeformed state of the blade
θ_0	root pitch angle
$\theta(x)$	blade pitch angle, at radial location x
$\theta_{tw}(x)$	built-in twist angle, at radial location x
$\phi(x)$	elastic twist angle, at radial location x
Ω	rotational rate

(*a*) Flexible rotor at rest, mounted on hover test stand

(*b*) Flexible blades rotating at 1500 RPM, stiffened by centrifugal forces

Figure 1. Extremely flexible rotor concept (46 cm diameter).

1. Introduction and motivation

Micro aerial vehicles have become increasingly popular over the past decade as they are capable of performing missions that conventional manned vehicles or larger unmanned aerial vehicles cannot. Their small size allows them to remain undetected and to penetrate confined areas, which makes them well suited to operate in caves or other indoor locations, primarily in a surveillance or reconnaissance role. Of particular interest is the concept of a revolutionary micro-helicopter equipped with extremely flexible rotor blades [1], which is advantageous for multiple reasons. First, the flexibility of the blades is such that they can be rolled up during operation, creating a variable rotor diameter depending on mission requirements. Second, in the event of collision with an object, the blades can deform and spring back to their original position, effectively creating a damage tolerant rotor. A proof-of-concept 46 cm diameter rotor with extremely flexible blades is shown at rest in figure 1(*a*) and rotating at 1500 RPM in figure 1(*b*). It can be seen that the stiffness of the blades is so low that they experience very large bending deflection at rest due to their own weight. Under rotation, the gravitational forces are overcome by centrifugal forces that stiffen and stabilize the rotor blade. However, centrifugal effects are also responsible for large torsional deformation (figure 1(*b*)) induced along the blade span, especially at high thrust, leading to poor efficiency. Sicard and Sirohi [1] described these effects and investigated different approaches to tailor the induced twist distribution. For example, a design making use of the propeller moment acting on a tip mass located at an index angle to the blade chord was tested and positive results were assessed based on a measured improvement in hover efficiency as well as visual observation of the deformed blade shape.

To further improve the design of a flexible rotor, a better understanding of the effects of the design parameters on the blade deformation is required. Consequently, an aeroelastic analysis capable of modeling unconventional rotors with very large deformations has been developed [2]. The present research is motivated by the need for detailed measurements of the flexible rotor blade deformation, to be used in the validation of the aeroelastic analysis. However, the experimental measurement of rotor blade deformation is a very challenging task. The conventional method using strain gages bonded to the blade surface at discrete spanwise locations is unsuitable for multiple reasons. First, this technique requires an extensive on-blade instrumentation and wiring, as well as an electric slip ring, which are not feasible at the scale of the present rotor. In addition, because of its limited spatial resolution, this technique is incapable of showing strain gradients and can miss strain hot spots. In the present case, where the shear moduli of the blade material and the strain gage are on the same order of magnitude, the presence of the installed gage may significantly alter the specimen strain distribution. Finally, measurement of extension, flap and lead-lag bending and torsion require four separate sets of strain gage installations, one for each of the measured quantities.

Due to these limitations, we consider optical techniques to measure the deformation of the flexible rotor blade. These techniques are very advantageous, as they are able to generate full-field deformations [3], without instrumenting the structure and in a non-contact fashion. Interest in optical deformation measurement techniques has been rising since the beginning of the 1990s. However, a limited number of studies exist on their application to the measurement of rotating blade and deformation. Fleming *et al* [4, 5] demonstrated the capability of projection moiré interferometry to measure azimuthal variations of rotor blade deflections at different advance ratios, in or out of fuselage influence. This study was extended to the test of a model-scale rotor in the NASA Langley 14 × 22 feet subsonic wind tunnel hover facility [6]. Olson *et al* [7] and Abrego *et al* [8] used stereo photogrammetry to measure the deformation of full-scale UH-60A helicopter blades at various advance ratios, thrust coefficients and drive shaft angles. The experiment used reflective circular targets attached at specific locations on the blade and produced results that closely matched the design parameters. Sirohi and Lawson [9] investigated the application of stereoscopic digital image correlation (DIC) to the measurement of flap bending and torsion of rotating micro-helicopter blades (diameters of 61 and 99 cm). This technique was found to be very attractive as it allows for three-dimensional contours as well as non-planar displacements and strains. In the DIC technique, a high-contrast random speckle pattern is painted on the rotor blades. Cross-correlation of the images at different loading conditions, in conjunction with photogrammetry, is used to calculate

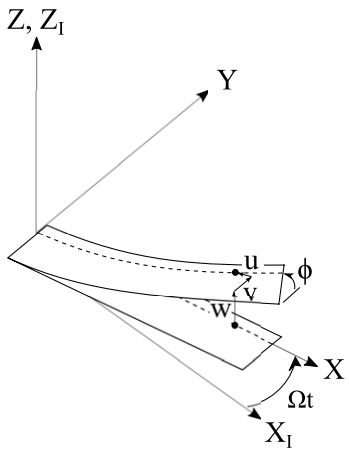

Figure 2. Blade coordinate system.

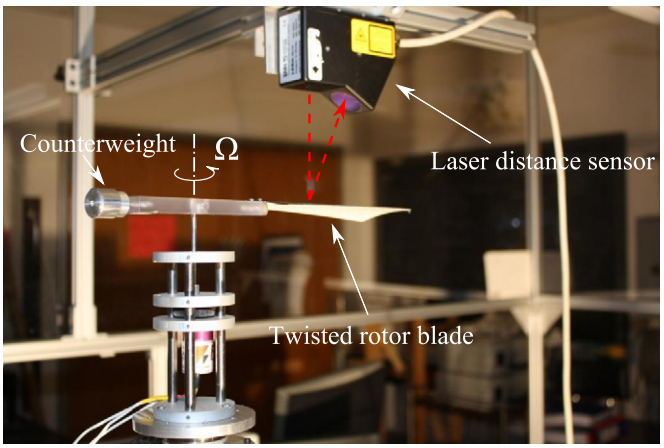

Figure 3. Stiff rotor blade mounted on the hover test stand.

three-dimensional displacements of points on the surface [10]. While the DIC technique was successfully validated in the non-rotating frame by measuring the deformation of a vibrating cantilever beam, no validation was performed in the rotating frame.

Sicard and Sirohi [11] extended this work to the measurement of flap bending and torsional deformation on a 46 cm diameter extremely flexible rotor.

From these studies, it was concluded that the DIC technique is very well suited to the measurement of flexible rotor blade deformation. However, to increase confidence in the technique, DIC measurements must be comprehensively validated in the rotating frame. This work has three goals. First, to validate the DIC technique in the rotating frame by correlating measurements with a laser distance sensor (LDS). Second, to make detailed measurements of the extension, flap and lead-lag bending and torsion of extremely flexible blades on a 46 cm diameter rotor. Finally, to discuss the scalability of the technique to the measurement of full-scale rotor blade deformation.

2. Measurement approach

The stereoscopic DIC technique enables the measurement of the three-dimensional shape of a rotating helicopter blade and the generation of whole-field, three-dimensional displacement vectors. From the displacement vector fields, the extension (u), lead-lag and flapwise bending deflections (v and w) and the elastic twist distribution along the span (ϕ), as defined in figure 2, are computed. Note that this coordinate system is defined with respect to the rotor hub, i.e., the Z-axis is aligned with the rotor shaft and the rotor hub lies in the X–Y plane.

The validation of the DIC measurements in the rotating frame was achieved through the following procedure. First, a stiff rotor blade of known geometry was tested and its shape as measured by DIC was compared to the shape of the mold from which it was made. At a constant radial station, DIC measurements of the surface height of the rotor blade were compared to measurements from a LDS mounted in close proximity to the spinning rotor. Note that such an arrangement is not practical for performance measurements because of transient loads introduced by the aerodynamic interference between the LDS and the rotor blade. Finally, the pitch angle at the root of the blade was measured by a laser inclinometer and compared to the pitch angle calculated from DIC measurements.

Once the DIC technique was validated on the stiff rotor blade, it was used to measure the surface heights of the flexible blades on the 46 cm diameter rotor. From these measurements, the spanwise distribution of the three components of displacement (u, v and w) as well as twist of the rotor blade (ϕ) was computed. The experiment was repeated at several blade pitch angles to generate a detailed set of experimental data for future correlation with the aeroelastic analysis.

3. Experimental procedures

3.1. Hover test stand and rotor blade designs

The rotor blades were tested on a vertical hover test stand with a rotor plane approximately 120 cm from the ground. The stiff blades and the flexible blades were spun on different test assemblies to accommodate their specific root geometry. For the tests involving the stiff blades, a 41.8 cm diameter, one-bladed rotor with counterweight was mounted on a rigid hub (figure 3), and spun by a brushless in-runner dc motor (Feigao 130) at rotational speeds varying from 300 to 900 RPM. The blade featured a constant chord of 50 mm, a thin circular arc airfoil and a linear twist distribution of -0.7° cm^{-1}. Blade pitch angles were manually set at values ranging from 0° to 15°. These blades were fabricated in-house by curing two plies of carbon fiber prepreg (AS4/3501) in a hot compression mold.

For the tests involving the flexible rotor blades, a 45.8 cm diameter rotor was mounted on a two-bladed rigid hub (figure 4), and driven by a brushless out-runner dc motor (Hacker A50 16S) at 1200 RPM. The flexible blades featured a constant chord of 23 mm and had a tungsten rod secured at the blade tip in a chordwise direction, for centrifugal stiffening and stabilization. The blades were fabricated in-house using a wet layup process with a carbon fiber cloth and a polyurethane matrix. Blade pitch was set using a conventional swashplate

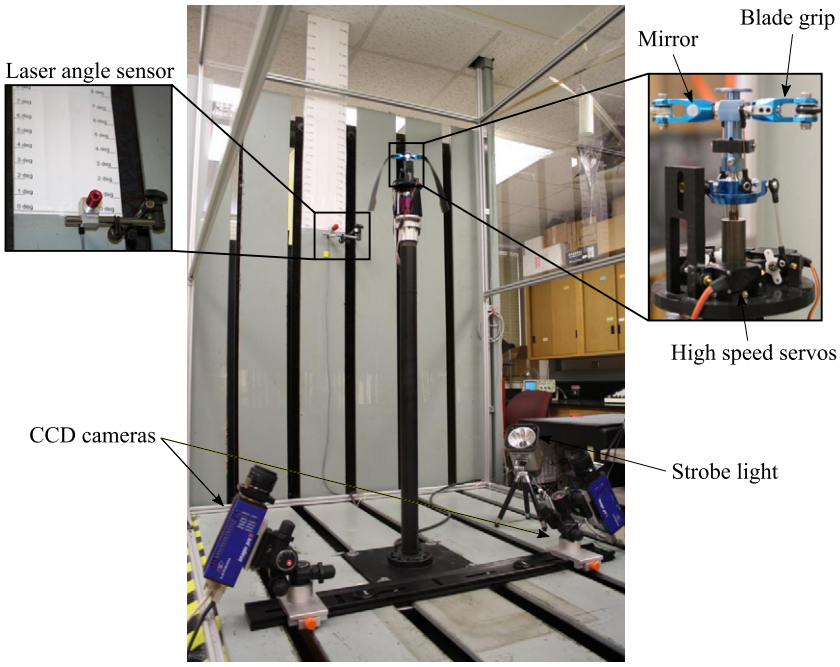

Figure 4. Extremely flexible rotor blades mounted on the hover test stand.

Table 1. Rotor blade parameters.

	Stiff blade	Flexible blade
Airfoil	Circular arc	Circular arc
Rotor radius R, m (in)	0.209 (8.228)	0.229 (9.016)
Chord c, mm (in)	50 (1.969)	23 (0.906)
Twist θ_{tw}, deg cm^{-1} (deg in^{-1})	−0.7 (−1.8)	–
Camber, Ca (% of c)	5.5	7.5
Thickness, t (% of c)	1.3	1.39
Tip body mass, g (oz)	–	2.05 (0.072)
Blade mass, g (oz)	7.48 (0.264)	4.30 (0.152)
Blade material	AS4/3501 prepreg	Carbon fiber cloth/ polyurethane matrix

assembly actuated by three high-speed digital servos. Table 1 summarizes the parameters of each blade design; more details on the blades and the hover test stand characteristics can be found in [1].

The rotational speed of both rotors was measured using a once-per-revolution (1/rev) optical switch. This 1/rev signal was also used to trigger other instruments.

3.2. Laser distance sensor

A high-frequency laser triangulation sensor (LMI LDS 80/10 M) was mounted on a fixture above the rotor plane to measure the blade surface height during rotation. Note that this sensor has a standoff distance of 80 mm; therefore, the sensor was mounted approximately at this distance above the rotor plane (shown in figure 3). The laser beam projected by the sensor was reflected from the top surface of the blade to a CCD array through a collection lens. This measurement device is able to sense distances from 0 to 10 mm with a resolution of 0.001 mm, a standard deviation of 0.01 mm and a bandwidth of 10 kHz. The output voltages were recorded by a 50 MHz digital oscilloscope, before being converted into distances based on the calibration constant. Note that this sensor gave a measurement only during the time when the rotor blade passed through the laser beam; during the remainder of the rotor revolution, the output of the sensor was zero.

3.3. Laser inclinometer

A laser inclinometer was constructed by attaching a mirror to the blade grips and reflecting a laser beam from it to a calibrated screen (shown in figure 4). This method was able to give a direct measurement of the rotor blade root pitch during rotation, in the range of 0° to 23° with an accuracy of 0.2°.

3.4. Digital image correlation technique

The three-dimensional DIC technique involves the preparation of the rotor blade surface, calibration of the camera setup and capturing images of the rotor blades during rotation. In the first step, the DIC setup is calibrated using a target of known geometry so that a mapping function is established between physical dimensions and the camera images. Second, images of the spinning rotor blade are captured at different loading conditions and at a specific azimuthal location. After the images are captured, the DIC software uses photogrammetry to create three-dimensional maps of the blade surface. Image correlation algorithms are then used to generate three-dimensional displacement vectors between the image of the deformed blade and a reference image. The DIC software used in this study was LaVision DaVis 7.2-StrainMaster 3-D. [12]. Finally, post-processing algorithms developed in-house were used to extract the extensional, flap and lead-lag bending as well as torsional deformation from the displacement vectors.

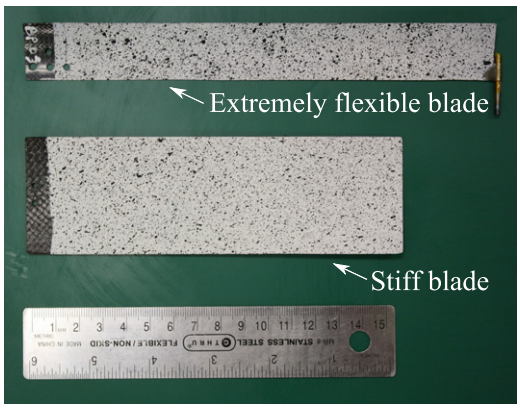

Figure 5. A high-contrast random pattern on the bottom surface of rotor blades.

3.4.1. Blade preparation. The lower surface of the rotor blades was prepared with a high-contrast random dot or speckle pattern (figure 5) such that points on the surface were easily distinguished. First, the surface was painted with a uniform matte white background. Then, a stiff-bristled brush dipped in matte black paint was used to spray a random pattern of fine black speckles on this background. This technique resulted in the generation of speckles varying in size from 0.15 to 1.95 mm, which was appropriate for the resolution of the raw images taken by the cameras (6.75 pixels per millimeter). In particular, the speckle size was chosen such that it was greater than the dimensions of one pixel, but less than the size of the interrogation window of the cross-correlation algorithm (32 × 32 pixels).

3.4.2. Digital cameras. The cameras (Imager ProX 2M) used for these experiments have a 1600 × 1200 pixel resolution, 29.5 Hz operation speed (15 Hz continuous), CCD image sensors and 16 384 (14 bit) gray levels. The exposure time is adjustable within the range of 500 ns to 1000 ms and the cameras are capable of accepting an auxiliary TTL triggering signal. The cameras were equipped with Nikon 50 mm AF NIKKOR f/1.8D lenses; these lenses do not have any zoom, have a minimum focal distance of 1.5 feet (0.45 m) and a variable aperture from f1.8 to f22. The cameras were placed below the rotor disk a fixed distance apart and were oriented such that the image of the rotor blade was aligned with the longer dimension of the CCD sensor, so that the maximum spatial resolution could be achieved. The arrangement of the two cameras with respect to the rotor stand can be seen in figure 4.

3.4.3. Calibration. A calibration procedure was performed to establish a mapping function between real-world dimensions and the camera image dimensions. This calibration procedure was crucial, as it defined the position and orientation of the cameras with respect to the test sample as well as a reference coordinate system in which all the output quantities were expressed. In addition, the calibration procedure produced a dewarping function correcting the image distortions due to perspective projections and inherent camera lens distortions.

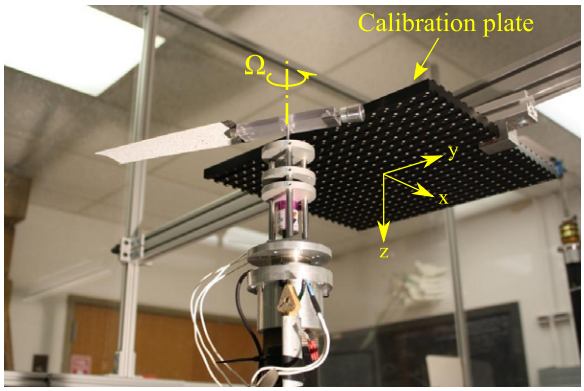

Figure 6. Reference system of axes defined during calibration.

In this study, a calibration plate was carefully aligned coplanar with the rotor hub plane, the x- and y-axes being aligned with the radial and tangential directions of the blade, respectively (figure 6). The z-axis was defined as the normal to the calibration plate, parallel to the rotor shaft. The calibration plate had an array of targets imprinted on its surface and in groove to give a three-dimensional collection of targets with a precisely known spacing. The dimensions of the plate (310 mm × 310 mm) were such that the target locations encompassed the x- and y-ranges of values occupied by the rotor blades during the experiments. Several images of the calibration plate were captured by both cameras. For each set of images, the target locations on the calibration plate were identified and their positions were used to calculate, using a pinhole model, the dewarping function and the mapping function between real-world coordinates and camera image coordinates. The resulting calibration was effectively valid everywhere in the volume that was in focus to the camera, i.e. the depth of field.

3.4.4. Image acquisition. After the DIC system was calibrated, images of the rotating blades were captured (figure 7). A 10 W xenon stroboscope, triggered once per revolution by a Hall effect sensor mounted on the rotor shaft, illuminated the blade at a fixed azimuthal position. The duration of the flash (10 μs) was short enough for the resulting camera images to appear motionless. To increase the intensity and contrast of the pictures and therefore produce more accurate correlation computations, the aperture of the cameras was kept open for 1 s, effectively adding up multiple passes of the blade on each image. The process was repeated at different settings of rotor blade pitch, resulting in a pair of images at each blade pitch. As the blade pitch increased, the aerodynamic loads on the rotor blade increased. The increased lift causes upward bending of the blade, increased drag causes lead-lag bending of the blade (against the direction of rotation) and aerodynamic pitching moments affect the twist distribution along the blade.

3.4.5. Computation of deformation. Using the raw images, the DIC software calculated a surface height map of the rotor blade and displacement fields. While the surface heights were computed relative to the absolute reference frame defined

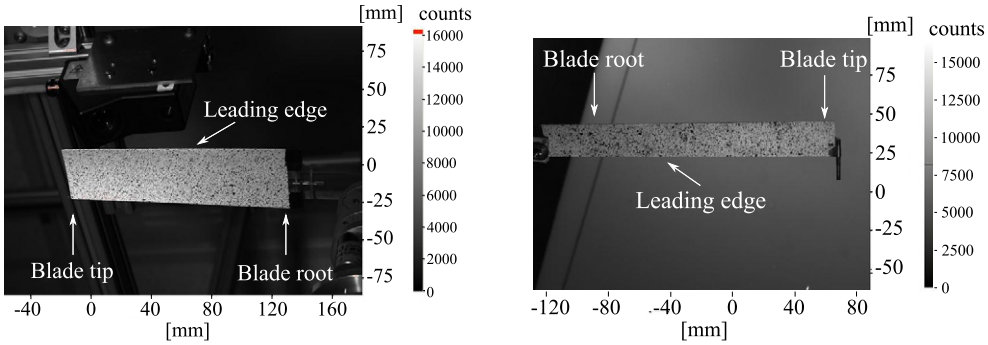

(*a*) Bottom surface of the stiff blade rotating at 900 RPM

(*b*) Bottom surface of the flexible blade rotating at 1200 RPM

Figure 7. Raw images acquired with the DIC system.

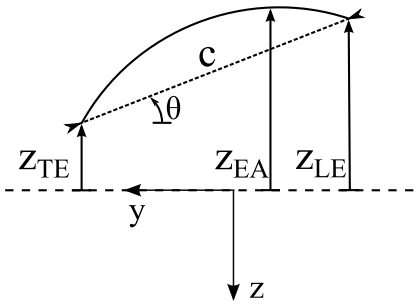

Figure 8. Surface heights of LE, TE and EA are extracted from DIC results.

during calibration, the displacements were obtained with respect to the position of the blade in the undeformed state, as defined by the first image of each data set.

To ensure that the azimuthal position of the blade in the undeformed and deformed states was the same, the undeformed state corresponded to the blade spinning at very low RPM. In addition, the blade root pitch at the undeformed state was set to zero. These two conditions were chosen such that deformations due to centrifugal and aerodynamic forces were negligible. It should be noted that this zero reference also eliminates the contribution of gravitational forces to the computation of blade deformations.

The surface height map generated by the DIC software was directly used to plot the blade shape at a given radial station. In addition, the displacement vectors of points located along the blade elastic axis (EA) were extracted from the global displacement fields in order to plot the blade extension and bending deflections. This way, displacements normal to the rotor disk plane due to the flap bending and in-plane displacements due to lead-lag bending deflection were decoupled from the displacements produced by the twist of the blade.

Finally, an algorithm was written to compute the spanwise variation of pitch angle. Using the surface heights of the leading edge (LE) and trailing edge (TE) of the blade, shown in figure 8, the local pitch was calculated as follows:

$$\theta(x) = \arcsin\left(\frac{z_{\mathrm{LE}} - z_{\mathrm{TE}}}{c}\right). \tag{1}$$

Then, the elastic twist could be computed by subtracting the blade root pitch angle (set for each test condition) and built-in structural twist from the measured local pitch:

$$\phi(x) = \theta(x) - \theta_0 - \theta_{\mathrm{tw}}(x). \tag{2}$$

3.4.6. Spatial resolution. The surface heights were calculated by the DIC software for each pixel of the raw images. For this study, this led to a spatial resolution equal to 0.15 mm or 0.06% of the rotor radius. Local pitch angles, which were computed using the surface heights of LE and TE, were obtained at the same resolution.

The displacement vectors were calculated for each interrogation window of the DIC algorithm which, in this study, consisted of squares of 32 × 32 pixels with a 50% overlap between two adjacent windows. Consequently, the spatial resolution of the displacement vector field was of 16 pixels (2.37 mm) or 1.04% of the rotor radius.

4. Results and discussion

In this section, a comprehensive validation of the DIC technique to measure three-dimensional rotor blade displacements is presented. Then, the full-field deformations of a 46 cm diameter extremely flexible rotor are measured.

4.1. Validation of the DIC technique

The surface heights of the stiff rotor blade at a fixed spanwise position (three-quarter span) were measured using the DIC technique and LDS. A comparison between the results of both techniques at three different rotational speeds (500, 700 and 900 RPM) is shown in figure 9. These measurements give not only the shape of the blade section but also its mean vertical position.

As the rotational speed increases, the increased lift on the rotor blade will cause it to bend upward. Because the blade is relatively stiff, negligible torsional deformation is expected. Based on the measured data, the first observation is that the DIC data are significantly smoother than the LDS data. Nevertheless, it can be seen that the measurements by DIC,

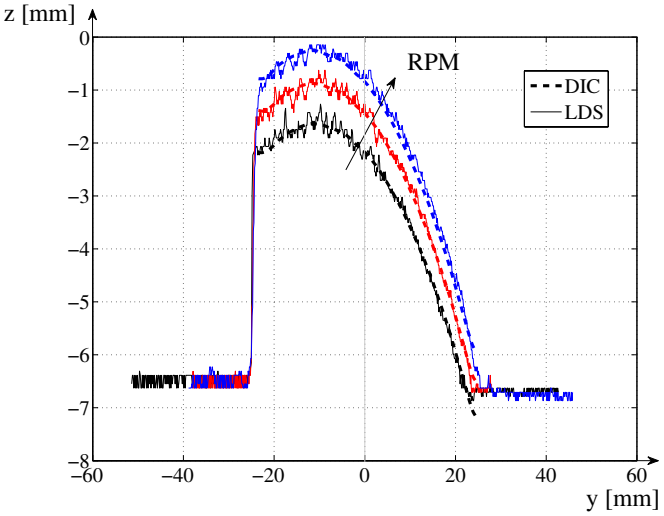

Figure 9. Blade section position and shape measured by DIC and LDS at 3/4 span of 21 cm stiff blade, $\theta_0 = 11^\circ$, $\Omega = 500$, 700 and 900 RPM.

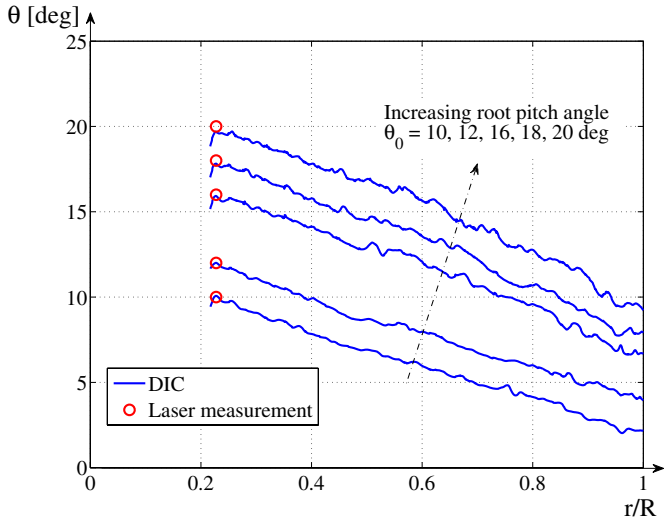

Figure 11. Spanwise variation of pitch along 23 cm flexible blade, measured by DIC and compared to measurement of root pitch angles by laser sensor, at Ω = 1200 RPM.

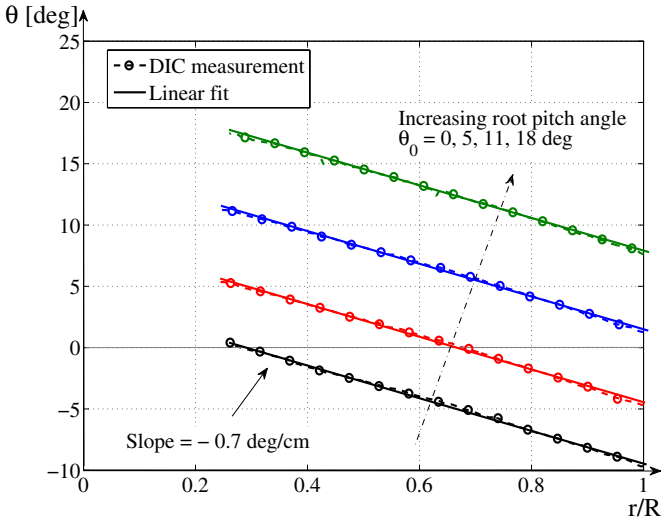

Figure 10. Spanwise variation of pitch measured by DIC, compared to design parameters (21 cm stiff blade, washout twist, -0.7° cm $^{-1}$), at various root pitch angles, Ω = 300 RPM.

plotted as dashed lines, are contained within the dispersion of the LDS data. Consequently, we conclude that both the DIC and LDS experimental techniques give an identical three-dimensional position in space and identical shape of the rotating blade, which proves that both methods are reliable. It should be added that the error relative to the computation of surface heights, as defined in the previous section, is equal to 0.1 pixels, which is equivalent to 0.015 mm for the present experiment.

In order to confirm the computation of blade pitch angles using DIC measurements, the experimental data were compared to the design of the mold used to fabricate the blade. Figure 10 shows the spanwise variation of pitch for the stiff blade rotating at 300 RPM, at various root pitch angles. A linear fit is applied to the experimental data and it is found that the slope of the straight lines is equal to -0.7° cm^{-1}, which corresponds to the actual structural twist of the blade imparted by the mold (as given in table 1). It can also be seen from this graph that the blade experienced negligible elastic twist deformations since the pitch at each radial station is approximately equal to the sum of the root pitch and the built-in twist ($\phi(x) = 0$ in equation (2)).

Furthermore, the pitch angle at the root of the 23 cm flexible blade, as computed from DIC measurements, is compared to the angle given by the laser inclinometer in figure 11. It is seen that both measurement techniques are in good agreement.

From these comparisons, we conclude that the DIC technique is a reliable approach to measure rotor blade deformation under rotation. Consequently, the DIC technique can be extensively used to generate the full-field displacements of various blade designs.

Figure 12 shows the flap bending deflections of the 21 cm twisted blade as a function of radial coordinate, at 10° root pitch and various RPM. As mentioned earlier, the displacements are not absolute, but instead relative to the shape of the blade at an arbitrary undeformed state defined when it is spinning at 300 RPM and at 10° root pitch.

4.2. Three-dimensional deformations of an extremely flexible rotor

Figure 13 shows the extension as well as the flap and lead-lag bending deflection associated with the flexible rotor blade, spinning at 1200 RPM. The extension and lead-lag bending were calculated relative to a reference state where the blade spun at 1200 RPM and at 10° root pitch. At slower RPMs or lower pitch angles, the flexible rotor experienced aeroelastic instabilities (pitch-flap flutter) responsible for blurred raw pictures preventing any DIC correlation. On the other hand, the absolute flap bending deflection (i.e. relative to the

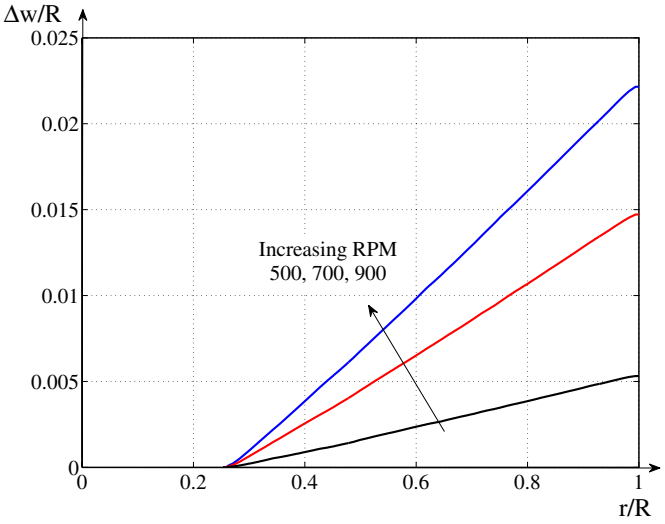

Figure 12. Flap bending deflection of 21 cm stiff blade, measured by DIC at 10° root pitch, Ω = 500, 700 and 900 RPM.

reference frame defined during calibration) could be computed by extracting the surface heights of points located on the blade EA. This operation was possible because the flexible blade was not structurally pre-twisted, and its undeformed (i.e., without the effect of gravity) EA was contained in the plane of the calibration plate. As a result, the flap bending deflections were the combined result of centrifugal, aerodynamic and gravitational effects, while the extension and lead-lag bending deflections were based on the reference condition. The measured twist distribution was also the result of combined centrifugal, aerodynamic and gravitational effects because it relied on the measurement of surface heights.

It can be seen (figure 13(*a*)) that as the blade pitch increases, the blade appears to decrease in length, i.e., the axial extension is negative and decreases. This effect is called axial foreshortening and is a kinematic consequence of the increase in blade bending and twist, defined by [11]

$$u_F(x) = -\int_{x_0}^{x} \left(\frac{v'^2}{2} + \frac{w'^2}{2} + \frac{c^2}{8}\phi'^2 \right) \mathrm{d}\chi. \qquad (3)$$

Note that this foreshortening effect arises because the extension is defined with respect to the hub-fixed coordinate system (figure 2).

The increase in lead-lag bending (figure 13(*b*)) and flap bending deflection (figure 13(*c*)) is the result of an increase in drag and lift with an increasing blade pitch. Since the direction for flap bending is defined as the normal to the plane of the rotor hub, it is affected by both the drag and the lift forces, which instead are parallel and perpendicular to the resultant local flow velocity, respectively. The same remark can be applied to the lead-lag bending deflection, whose direction is defined to be coplanar with the rotor hub plane, normal to the undeformed blade span.

Additionally, we can compare the orders of magnitude of the normalized displacements in the three directions. The magnitude of the extension is negligible compared to the magnitude of bending deflections. However, normalized lead-lag and flap bending deflections have similar orders of

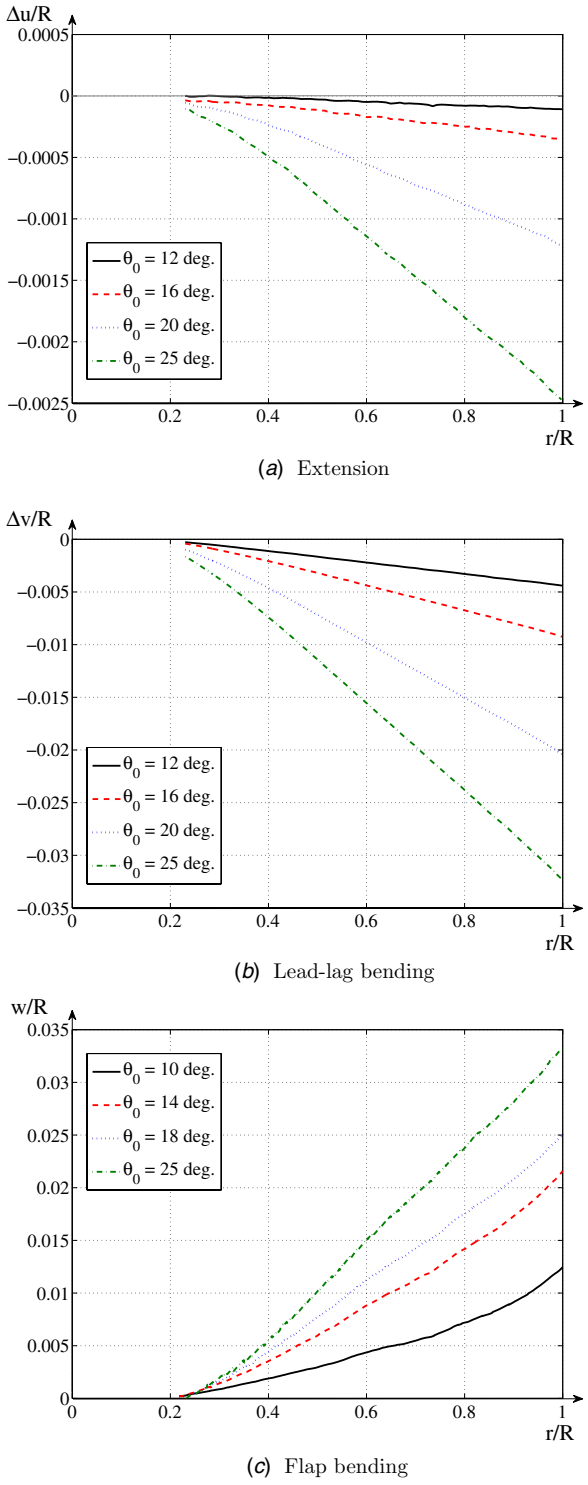

Figure 13. Deformations of 46 cm diameter flexible blade, measured by DIC at Ω = 1200 RPM.

magnitude, which indicates that in order to accurately model such a rotor blade, both lead-lag bending and flap bending degrees of freedom must be taken into account.

Finally, the elastic twist of the flexible blade as a function of radial coordinate can be obtained by subtracting the blade root pitch angle from the measured local pitch shown in figure 11 (the built-in structural twist being equal to zero). The magnitude of the resulting elastic twist is comprised between

0° and -10.8°. This implies that unlike conventional rotor blades, the elastic twist in the case of an extremely flexible rotor blade is of the same order of magnitude as the root pitch angle.

4.3. Error analysis

It is important to determine the accuracy of the measurements obtained using DIC to compare the method with alternative experimental techniques. An estimation of the uncertainties in the DIC measurement based on a literature survey is presented. Then, the calculation of the error from the recorded experimental data is given.

The manual delivered with the La Vision DaVis 7.2 software package [12] gives an estimate of the accuracy of the displacement vectors computed by the DIC algorithm. This estimate is only a function of the size of the interrogation window used by the algorithm and holds for an ideal experimental setup with high-quality images, high-contrast speckle pattern and perfect calibration procedure. In this study, the size of the interrogation window was 32×32 pixels and the resolution of the images was 6.75 pixel mm^{-1}. The corresponding accuracy of the 3D vectors as indicated by the manual is of 0.05 pixels, which translates to an absolute accuracy of 7 μm.

However, there are other sources of error in the computation of displacement vectors than those produced by the DIC algorithm. Several studies have focused on quantifying overall measurement accuracy in a 3D DIC setup [13, 14]. Classically, the sources of error are divided into two categories. The first one relates to the correlation process, which is linked to the quality of the speckle pattern, the interrogation window size and correlation algorithms such as interpolation of grayscale intensities [15]. The second type of error affects the 3D reconstruction of the test specimen and is due to uncertainties in the relative position and orientation of the cameras with respect to the calibration plate. Based on this literature survey, for the present setup, the combined error due to all sources of uncertainty is on the order of 0.01 pixels (1.5 μm) for in-plane displacements and 0.1 pixels (15 μm) for out-of-plane displacements.

In addition, the accuracy of the DIC technique can be estimated from the comparison of displacement measurement carried out with the LDS and the DIC system. It was found that the standard deviation between the LDS data and DIC data (shown in figure 9) was equal to 120 μm. However, the uncertainty in LDS measurements is dominated by electrical noise, which is absent in the DIC measurements. Therefore, we conclude that the DIC measurements are at least as accurate as the laser displacement sensor.

Finally, the repeatability of the DIC experimental procedure was investigated. The DIC technique used raw images composed of a number of exposures of the rotor blade at a specific azimuthal location. Hence, the uncertainty in the measurements is dominated by the random variations in the rotor blade displacement from one revolution to another due to turbulence. However, it was noted that these variations were small and did not cause a notable blur when the images were superimposed. Another issue with repeatability is when the camera setup is changed and the experiment is repeated. Guidelines for alignment and spacing of the cameras result in very small variations in the setup of cameras between experimental runs and it was noted that there is no observable difference in the measured results. Therefore, we conclude that the error associated with repeatability is below the uncertainty of the DIC technique.

5. Discussion on the scalability of the DIC technique

Although the experimental validation of the DIC technique to the measurement of rotor blade deformations was demonstrated on reduced-scale rotors, the method can be scaled and applied to the testing of full-scale rotor blades. The first recommendation is to adjust the size of the speckle pattern to the resolution of the raw images. In addition, a higher intensity light source, for example, a laser strobe, is required to illuminate the increased area. Finally, the calibration of the DIC system must cover an area as large as the rotor blade, which makes the use of a calibration plate impractical. Instead, targets separated by known distances can be placed on the ceiling of the testing facility and identified by the DIC software. For example, consider a Mach-scale rotor of diameter 4 m. Assuming that the same camera setup with the same optics as described in this paper is used, the cameras must be located at a distance 11.3 m away from the rotor plane to capture an image of the entire rotor blade, and the blades must be painted with a speckle of nominal size of 10 mm. This will result in an image resolution of 8 pixels per centimeter which will translate to a spatial resolution of the computed displacement vector field of 20 mm and an accuracy of 125 μm. The spatial resolution and accuracy can be improved by changing the optics on the cameras, changing the size of the camera CCD sensor and also by capturing only a portion of the rotor blade and subsequently stitching the images together. However, in the latter case, errors may be easily introduced by repositioning of the cameras and during the stitching algorithm. We conclude that even with capturing the entire rotor blade in one image, the DIC technique will yield accurate measurements with a much higher spatial resolution than conventional strain gage measurements.

6. Summary and conclusions

The goal of this paper was to present the measurement of the deformation of an extremely flexible helicopter blade using stereoscopic digital image correlation (DIC). This blade is so flexible that it can be rolled up into a compact volume. The measurement technique was first validated on a 21 cm stiff blade of known geometry through a comprehensive set of experiments. Key parameters to ensure accurate DIC were identified:

(i) the surface of the test specimen must be prepared with a high-contrast random speckle pattern of size adjusted to the resolution of the raw images;

(ii) bright and blur-free images can be obtained by using a strobe light to freeze the rotor blade at a single azimuthal position, and by keeping the camera shutter open for a set time;

(iii) the calibration procedure is critical as it defines a 'real-world' reference frame in which all the output quantities are expressed, and with respect to which position and orientation of each camera are calculated.

The validation of the deformation of the stiff blade obtained by DIC in the rotating frame was achieved by comparing the full-field DIC data to local measurements acquired with auxiliary devices. A laser distance sensor was used to generate the shape and surface heights at a given radial station of the blade. These results closely matched the DIC data extracted at the same radial location. In addition, a laser inclinometer allowed the verification of the blade root pitch angle measured by DIC.

Once validated, the DIC technique was used to generate full-field measurements of extension, lead-lag and flap bending deflection and pitch angle of a 46 cm diameter extremely flexible rotor. Three-dimensional displacement vectors were obtained with a spatial resolution of 2.37 mm (1.04% of the rotor radius) and at an accuracy of 15 μm. It was found that the extension is mainly associated with kinematic foreshortening, and that lead-lag and flap bending deflections have comparable orders of magnitude. In addition, elastic twist angles were found to be of the same order of magnitude as root pitch angles. These observations indicate that the analysis of a flexible rotor must be tailored to rotor blades experiencing high twist deformations, with flap and lead-lag bending as well as twist degrees of freedom.

Finally, it was shown that the DIC technique can be scaled and applied to the testing of full-scale rotor blades. The size of the speckle pattern painted on the blade surface must be increased and adjusted to the resolution of the images of the full-scale blade. In addition, the intensity of the light source must be increased, for example by replacing the xenon strobe used in this study by a laser strobe.

In conclusion, the DIC technique was proven to be a reliable accurate method of measuring large deformations of rotating blades. Future effort will involve extending the use of the DIC technique to the measurement of unsteady rotor blade deformation and to the computation of rotating natural frequencies and mode shapes.

References

[1] Sicard J and Sirohi J 2012 Experimental study of an extremely flexible rotor for microhelicopters *J. Aircr.* **49** 1306–14

[2] Sicard J and Sirohi J 2012 Modeling of the large deformations of and extremely flexible rotor blade *European Rotorcraft 38th Forum Proc. (Amsterdam, The Netherlands, 4–7 Sept.)*

[3] Schmidt T, Tyson J and Galanulis K 2003 Full-field dynamic displacement and strain measurement using advanced 3D image correlation photogrammetry: part I *Exp. Tech.* **27** 47–50

[4] Fleming G A and Gorton S A 2000 Measurement of rotorcraft blade deformation using projection moiré interferometry *Shock Vib.* **7** 149–66

[5] Fleming G A, Soto H L and South B W 2002 Projection moiré interferometry for rotorcraft applications: deformation measurements of active twist rotor blades *American Helicopter Society 58th Annu. Forum Proc. (Montreal, Canada, 11–13 June)*

[6] Sekula M 2012 The development and hover test application of a projection moiré interferometry blade displacement measurement system *American Helicopter Society 68th Annu. Forum Proc. (Fort Worth, TX, 1–3 May)*

[7] Olson L E, Abrego A I, Barrows D A and Burner A W 2010 Blade deflection measurements of a full-scale uh-60a rotor system *American Helicopter Society Aeromechanics Specialist' Conf. Proc. (San Francisco, CA, 20–22 Jan.)*

[8] Abrego A I, Olson L E, Romander E A, Barrows D A and Burner A W 2012 Blade displacement measurement technique applied to a full-scale rotor test *American Helicopter Society 68th Annu. Forum Proc. (Fort Worth, TX, 1–3 May)*

[9] Sirohi J and Lawson M S 2012 Measurement of helicopter rotor blade deformation using digital image correlation *Opt. Eng.* **51** 043603

[10] Kahn-Jetter Z L and Chu T C 1990 Three-dimensional displacement measurements using digital image correlation and photogrammic analysis *Exp. Mech.* **30** 10–16

[11] Sicard J and Sirohi J 2012 Prediction and measurement of the deformations of an extremely flexible rotor using digital image correlation *American Helicopter Society 68th Annu. Forum Proc. (Fort Worth, TX, 1–3 May)*

[12] La Vision 2010 *DaVis StrainMaster 3-D, Software Package Version 7.2* La Vision, Göttingen, Germany

[13] Siebert T, Becker T, Spiltthof K, Neumann I and Krupka R 2007 High-speed digital image correlation: error estimations and applications *Opt. Eng.* **46** 051004

[14] Sharpe W N Jr 2008 *Springer Handbook of Experimental Solid Mechanics* (New York: Springer) pp 581–5

[15] Schreier H W, Braasch J R and Sutton M A 2000 Systematic errors in digital image correlation caused by intensity interpolation *Opt. Eng.* **39** 2915–21